J. Appl. Comput. Mech., xx(x) (2026) 1-15
DOI: 10.22055/jacm.2026.49649.6131

ISSN: 2383-4536
jacm.scu.ac.ir

Shahid Chamran
University of Ahvaz

Journal of
Applied and Computational Mechanics

Research Paper

Law-Dependent Cohesive-Zone Scaling in Mode-I Double-Cantilever-Beam Debonding

Marc Azab

College of Engineering and Technology, American University of the Middle East, Egaila, 54200, Kuwait, Email: marc.azab@aum.edu.kw

Received July 29 2026; Revised September 16 2026; Accepted for publication September 22 2026.
✉ Corresponding author: M. Azab (marc.azab@aum.edu.kw)

Abstract. Traction–separation laws with the same initial stiffness, strength, and fracture energy can give similar global double-cantilever-beam (DCB) responses but very different process zones. This study quantifies how post-peak law shape affects the debonding-onset process-zone length L_0 and its scaling. Six Mode-I laws (rectangular, linear, trapezoidal, finite exponential, quadratic, and multilinear) were compared in 100 Abaqus/Standard simulations spanning strength, fracture energy, arm height, and penalty stiffness, with L_0 measured at a common, interpolated onset event. Where a closed-form beam-on-cohesive-foundation solution exists at h = 1.6 mm, linear-law onset loads match it within 1%. Across 16 six-law blocks, the onset-load spread was 1.9–11.8%, whereas the L_0 spread was 116–258%, 19–98 times larger, partly owing to the shared fracture energy. The reference-block onset loads lie 11–16% below the beam-theory value, with a deficit that grows with L_0. The ranking of L_0 never changed, but the fitted exponents depended on the law. Expressed as local slopes of the scaling function, all eighteen estimates fell within the [1/4, 1] bracket of the slender-beam and bulk limits, indicating a shape-dependent crossover governed by the cohesive-length-to-height ratio. Adjacent-point slopes confirm this trend and always separate the largest-area from the smallest-area laws, although area, energy centroid, and final separation vary together. The beam shape coefficient varied with height (coefficient of variation 24–44%), while penalty-stiffness and onset-threshold effects stayed below 1% and 5%. Matching global curves does not ensure local equivalence, and law shape must be considered in parameter identification and mesh design.

Keywords: Cohesive-zone model, Traction–separation law, Double-cantilever beam, Process-zone length, Interface debonding, shape effect, Cohesive-zone scaling.

1. Introduction

Cohesive-zone models replace the singular crack-tip representation by a finite region in which separating surfaces continue to transmit tractions. Originating from the cohesive crack concepts of Barenblatt and Dugdale [1, 2], the approach now provides a unified finite-element description of damage initiation, softening, energy dissipation, and complete interface separation. Its appeal is accompanied by a well-known modeling ambiguity: a traction–separation relation must be selected even when the available experiments constrain only a limited set of global quantities. The range of formulations, calibration choices, and numerical consequences is reviewed by Park and Paulino [3].

For monotonic Mode-I separation, the constitutive input is commonly summarized by an initial penalty stiffness K_0, a maximum traction $T_{\max}$, and a critical fracture energy G_c. These quantities fix the initial slope, peak, and total area of the law but do not determine how traction is distributed over the post-peak separation path. They do define the characteristic cohesive length $\ell_{ch} = E'G_c/T_{\max}^2$, in which $E' = E/(1-\nu^2)$ is the plane-strain adherend modulus [4], which sets the order of magnitude of the process zone, but the dimensionless profile of the softening branch remains free. Treating the residual shape as a secondary numerical choice is therefore an additional assumption, not a consequence of matching K_0, $T_{\max}$, and G_c.

Published shape comparisons give decidedly mixed evidence. Chandra et al. [5] reported materially different metal–ceramic interface predictions for exponential and bilinear laws. In a controlled comparison, Alfano [6] showed that both law shape and structural stiffness affect the response and convergence of cohesive-zone simulations. Gustafson and Waas [7] found a weaker influence on the global responses of the double-cantilever-beam (DCB), end-notched flexure, and lap-joint configurations considered in their study. Campilho et al. [8] and Zhang et al. [9] subsequently showed that the preferred triangular, trapezoidal, or exponential form depends on the joint geometry and whether the adhesive response is brittle or ductile. The same ambiguity governs externally bonded FRP–concrete interfaces, one of the largest application fields of cohesive-zone modeling, in which bilinear, trapezoidal, and exponential bond–slip laws are routinely identified from global test data alone [10], and in which the same law-shape question has been shown to persist under mixed-mode debonding [11]. Selection by best global fit is standard practice in adhesive modeling more broadly: Simon Portillo et al. [12] compared candidate hyperelastic forms for flexible adhesives, retained the one that fitted the characterization tests most closely, and validated it against the global response of single-lap joints. Shape selection remains an active modeling question: mechanism-based multilinear laws continue to be proposed for Mode-I laminate fracture and fiber bridging [13, 14], new failure-mechanism-based traction–separation forms continue to be introduced for other interface systems [15], and the sensitivity of delamination predictions to the assumed cohesive description remains under active assessment [16, 17]. Collectively, these studies show that shape sensitivity is regime-dependent; they do not justify a generally negligible shape effect.

The same question arises, in a different guise, in regularized continuum fracture. Phase-field formulations replace the discrete interface by a diffuse band whose width is governed by a regularization length, and a substantial effort has been directed at removing or bounding the resulting sensitivity of the predicted response to that length [18]. The cohesive counterpart of that length is the process zone itself, and the shape of the softening branch is the modeling freedom that sets it. The question addressed here—how much of the local length scale is fixed by the calibrated global quantities, and how much is left to the assumed shape—is therefore the cohesive-zone analogue of the length-scale sensitivity question in phase-field fracture.

The distinction between global and local observables is central to this problem. Valoroso and de Barros [19] found nearly coincident DCB load–deflection curves for bilinear and exponential laws in a slender specimen while the corresponding cohesive-zone lengths remained different; increasing the arm thickness amplified both effects. The same distinction arises in adhesion testing: Sauvage et al. [20] found that the global rupture load of a three-point bending specimen had to be supplemented by the computed interface-normal stress field before the location and size of the initiation zone could be predicted, and proposed a local criterion on that basis. Analytical and numerical studies further show that cohesive-zone length depends on strength, toughness, penalty stiffness, adherend kinematics, specimen dimensions, and the adopted definition of the active zone [21–27]. The local field is also directly relevant to mesh design: the interface-element length must resolve the active zone rather than merely reproduce the global peak load [28, 29], a constraint severe enough that element formulations have been developed specifically to relax it [30]. The same tension between interface resolution and computational cost governs ply-level laminate models, in which every ply and every interface is discretized explicitly and the interface elements carry the delamination response [31].

Recent DCB identification studies reinforce this global–local distinction. Methods based only on load and opening can identify a prescribed bilinear model efficiently [32], but different cohesive parameters may still produce similar global curves [33]. Shape-free or full-field approaches therefore supplement the global response with crack-tip opening, energy-release-rate, or digital-image-correlation measurements [34–36]. These studies demonstrate why a validated global curve need not uniquely constrain either the traction–separation path or the spatial extent of the process zone.

The literature reviewed above leaves a specific gap. Existing shape studies typically compare two or three laws over one material–geometry setting, whereas cohesive-zone scaling studies usually adopt one fixed law and assign shape dependence to an empirical coefficient. Differences in onset definition, parameter range, and completeness of the law blocks further prevent a direct test of whether shape changes the exponents themselves. Consequently, two questions remain open. First, it is not known whether several laws sharing identical K_0, $T_{\max}$, and G_c also share common strength, energy, and structural-size exponents. Second, the local spread in cohesive-zone length has not been systematically compared with the simultaneous spread in global onset load at a common, reproducibly defined debonding-onset event.

The present study addresses this gap through a controlled 100-case numerical campaign containing six post-peak law families. Its purpose is to determine whether law shape can be represented by a transferable multiplicative factor or instead changes the sampled process-zone scaling itself. Relative to the shape-comparison and cohesive-zone-length literature, the contribution is the combination of three elements not previously brought together: a complete six-law design in which every law shares K_0, $T_{\max}$, and G_c within each of 16 parameter blocks, so that shape is the only variable inside a block; a single interpolated debonding-onset event at which the local length and the global load are extracted from the same analysis; and a scaling analysis that tests, rather than assumes, whether shape enters only through a multiplicative coefficient. Earlier studies compared two or three laws at one setting or fitted one law across settings; neither design can show that shape changes the exponents themselves, which is the central result here. The analysis uses a bracketed and interpolated debonding-onset definition, compares common and law-specific slopes descriptively, recasts the three one-factor exponents as local slopes of a single dimensionless process-zone function so that they can be compared with one another and with the two limiting regimes, compares global and local shape sensitivities, examines post-peak area and energy centroid as continuous descriptors, and checks the influence of penalty stiffness and onset threshold. This design is intended as a numerical isolation study: it establishes which differences arise from the assumed monotonic law shape before experimental identification, mixed-mode coupling, rate dependence, or plastic adherends are introduced.

The coefficient-only hypothesis tested in the campaign is:

$$L_0^{(j)} = C_j \left(\frac{E' G_c}{T_{\max}^2}\right)^{1/4} h^{3/4}, \tag{1}$$

where j denotes the cohesive-law family and $E' = E/(1-\nu^2)$ for plane strain. At fixed E', G_c, and h, Eq. (1) predicts $L_0 \propto T_{\max}^{-1/2}$. At fixed E', $T_{\max}$, and h, it predicts $L_0 \propto G_c^{1/4}$. These beam-regime exponents differ from the bulk limit, in which the process zone scales directly with ℓ_{ch} and therefore with $T_{\max}^{-2}$ and G_c^1 [4]. Related beam and crossover formulations make clear that Eq. (1) is a limiting scaling rather than a universal finite-DCB law, and that a finite specimen samples the transition between the two limits [21, 25, 26]. The numerical campaign tests whether the sampled exponents are shared by all shapes and whether C_j remains stable as the geometry changes.

A more general dimensionless statement follows from the governing set $(E', G_c, T_{\max}, h, a_0, K_0)$, in which a_0 is the initial crack length. These six quantities involve two independent dimensions, so the response is controlled by four dimensionless groups:

$$\frac{L_0^{(j)}}{h} = F_j(\Lambda, \eta, \kappa, \tau), \qquad \Lambda = \frac{\ell_{ch}}{h}, \quad \ell_{ch} = \frac{E' G_c}{T_{\max}^2}, \quad \eta = \frac{a_0}{h}, \quad \kappa = \frac{K_0 h}{E'}, \quad \tau = \frac{T_{\max}}{E'}. \tag{2}$$

The strain-magnitude group τ is retained for completeness because the analyses are geometrically nonlinear; it spans only 3.6×10^{-4}–1.1×10^{-3} across the present campaign, and Section 7.1 shows that the results are consistent with its omission, so that F_j is effectively a function of Λ, η, and κ alone in the small-strain regime sampled here. Poisson's ratio and the bonded length are the same in all analyses. The ratio of bonded length to arm height therefore still changes, from 43.75 to 2.19 in the height sweep, so the results hold for this bonded length only. Equation (1) corresponds to a particular asymptotic form of F_j: with $F_j \propto \Lambda^{1/4}$ it reproduces the slender-beam result, whereas $F_j \propto \Lambda^1$ reproduces the bulk limit $L_0 \propto \ell_{ch}$. The two limits therefore bracket the local logarithmic slope:

$$s_j = \frac{\partial \ln F_j}{\partial \ln \Lambda}, \qquad 1/4 \le s_j \le 1, \tag{3}$$

and a finite specimen is expected to sample intermediate values. The bracket follows from the two limiting regimes and is used as a physically motivated frame for the measured slopes; it is not a proof that every intermediate slope lies inside it, nor that $\ln F_j$ is concave everywhere. This observation is used in Section 7.1 to place the three one-factor sweeps on a common footing.

2. Cohesive-Law Family and Fair-Comparison Constraint

All six laws use the same linear-elastic branch up to:

$$\delta_0 = \frac{T_{\max}}{K_0}. \tag{4}$$

The normalized post-peak coordinate is:

$$\xi = \frac{\delta - \delta_0}{\delta_f - \delta_0}, \qquad 0 \le \xi \le 1, \tag{5}$$

and the post-peak traction is $T = T_{\max} f_j(\xi)$. If:

$$A_j = \int_0^1 f_j(\xi)\, \mathrm{d}\xi, \tag{6}$$

then the final separation is calculated independently for each law from:

$$\delta_f = \delta_0 + \frac{G_c/T_{\max} - \delta_0/2}{A_j}. \tag{7}$$

This condition ensures that the area beneath every complete law is exactly G_c. Holding a common final separation instead would confound the effect of shape with a change in fracture energy.

The six laws of Table 1 were not selected as a catalog of popular formulations but as a designed spread in the normalized post-peak area, which ranges from $A_j = 0.193$ for the finite exponential law to $A_j = 1.000$ for the rectangular law, a factor of 5.2. Because Eq. (7) maps A_j inversely onto δ_f, the same selection spans a factor of 5.2 in final separation at fixed G_c and $T_{\max}$. The set therefore samples the available post-peak design space approximately uniformly in $\ln A_j$ rather than clustering around the bilinear form, which is what makes a shape descriptor testable at all. Within the selected six-law family, a change of shape under the fair-comparison constraint is therefore inseparable from a change of final separation and of the distribution of dissipated work along the separation path; Section 8 returns to this point. The six laws are shown in both physical and normalized form in Fig. 1.

The normalized post-peak energy centroid is:

$$\chi_j = \frac{\int_0^1 \xi\, f_j(\xi)\, \mathrm{d}\xi}{\int_0^1 f_j(\xi)\, \mathrm{d}\xi}. \tag{8}$$

It measures where the post-peak cohesive work is concentrated along the separation path. Low values correspond to early traction loss; high values correspond to traction retention toward final separation. The analysis will test whether A_j and χ_j provide useful continuous descriptors of shape. Because A_j determines the law-specific δ_f through Eq. (7) and co-varies with χ_j in the selected six-law set, any centroid correlation is interpreted as exploratory rather than causal.

3. Finite-Element Model

The specimen is a symmetric two-dimensional DCB with a 30 mm traction-free precrack and a 70 mm bonded interface. The original crack tip is at $x = 0$, so the model extends from $x = -30mm$ at the loading end to $x = 70mm$ at the clamped end. Each arm has height h, unit out-of-plane thickness, Young's modulus $E = 100GPa$, and Poisson's ratio $\nu = 0.30$. Plane-strain four-node quadrilateral elements (CPE4) represent the arms. Plane strain is adopted as an idealization of the central region of a specimen whose width is large compared with its arm height, where the interface opening is uniform across the width; it is also the assumption under which E' enters Eqs. (1) and (2), so that the model and the analytical limits share one modulus. The unit out-of-plane thickness is a normalization: every load in this paper is a load per unit width, and no reported quantity depends on the absolute width. Anticlastic bending and free-edge effects in narrower specimens lie outside the model; no plane-stress or three-dimensional comparison was performed. The bonded interface is represented by four-node, zero-thickness user elements (UELs) with two Gauss points. The geometry and the near-interface mesh are shown in Fig. 2.

Table 1. Cohesive-law definitions and normalized post-peak descriptors.

Tag	Law	Normalized post-peak function $f_j(\xi)$	A_j	χ_j
REC	Rectangular	1	1.0000	0.5000
LIN	Linear	$1-\xi$	0.5000	0.3333
TRAP	Trapezoidal	1 for $\xi \le 0.5$; $2(1-\xi)$ otherwise	0.7500	0.3889
EXP	Finite exponential	$(e^{-5\xi} - e^{-5})/(1-e^{-5})$	0.1932	0.1824
POLY	Quadratic	$(1-\xi)^2$	0.3333	0.2500
MULTI	Multilinear	knee at $(\xi, f) = (0.30, 0.20)$	0.2500	0.2333

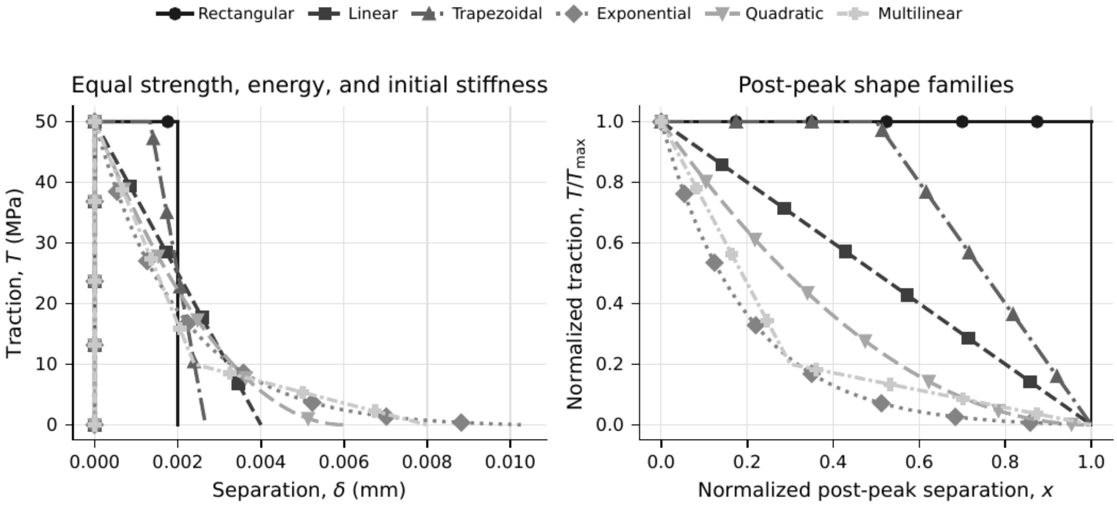

Fig. 1. The six cohesive laws in physical and normalized form, all with the same $T_{\max}$, G_c, and K_0.

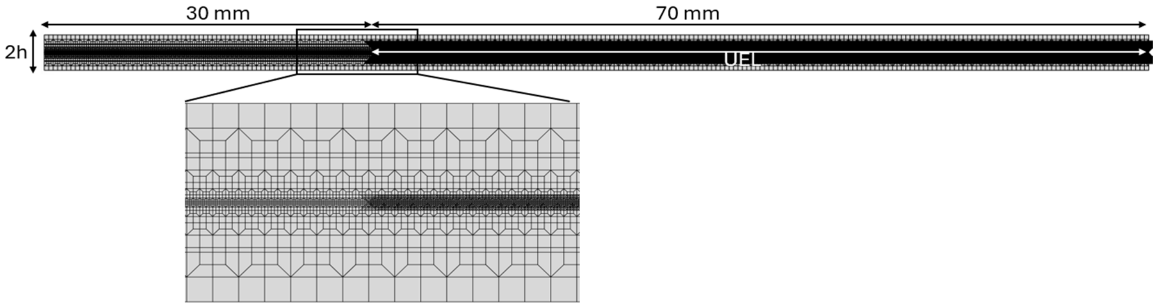

Fig. 2. DCB model with the 30 mm precrack, 70 mm bonded length, total depth $2h$, and zero-thickness UEL row; the inset shows the graded mesh near the interface.

The arm meshes conform to the interface nodes. The bonded 70 mm length is divided uniformly into 2,800 zero-thickness UELs, giving an interface-element length $\Delta x = 0.025mm$. This same longitudinal pitch is retained at the adjoining arm edges. Because the arm height is varied, the bulk mesh grows from 39,000 CPE4 elements and 43,272 nodes at $h = 1.6mm$ to 48,500 CPE4 elements and 52,810 nodes at $h = 32.0mm$. Each model additionally contains the same 2,800 interface elements; thus, the total element counts ranges from 41,800 to 51,300. The $h = 3.2mm$ reference model contains 39,500 CPE4 elements, 2,800 UELs, and 43,774 nodes.

The complete right edge at $x = 70mm$ is clamped. Mode-I opening is applied through the two single-node loading sets at $(x, y) = (-30mm, \pm h)$. The upper node receives $U_2 = +1mm$ and the lower node $U_2 = -1mm$ at the nominal end of the step, corresponding to a total prescribed opening of 2 mm; in practice, each job is stopped after the debonding-onset threshold has been bracketed. No force magnitude is prescribed. The applied opening Δ and the load per unit width P are recovered from the two loading nodes as:

$$\Delta = U_2^{\text{top}} - U_2^{\text{bottom}}, \qquad P = \frac{|RF_2^{\text{top}}| + |RF_2^{\text{bottom}}|}{2}. \tag{9}$$

Geometric nonlinearity is retained in an Abaqus/Standard 2022 static-general step. The prescribed opening is ramped linearly over a step period of 200 with an initial increment of 0.001, a maximum of 0.4 (0.004 mm of applied opening), a minimum of 10^{-20}, and up to 100,000 increments, so that the softening response is followed through the onset bracket; up to 30 cutbacks per increment are allowed, and the Newton iterations use the material tangent returned by the user element, which omits the derivatives of the element's deformed-configuration rotation. The element contains no viscous or otherwise rate-dependent term, so the only possible source of artificial damping is the solver, and none was used in 97 of the 100 analyses; the three exceptions, their post-onset stabilization-energy diagnostics, and a linear-geometry rerun of the baseline are reported in Section 7.

A single Abaqus/Standard UEL implements all six laws. The law is selected by LAW_ID, while the element assembly, coordinate transformation, integration rule, residual vector, and constitutive-tangent implementation remain unchanged. The property sequence is $(T_{\max}, G_c, \delta_0/\delta_f, \text{thickness}, \texttt{LAW\_ID})$.

The element implementation is checked against an independent analytical bound: the computed onset loads for all six laws are compared with the linear-elastic fracture-mechanics (LEFM) simple-beam value $P_{\text{LEFM}} = \sqrt{E'G_c h^3/(12a_0^2)}$ at $G = G_c$, reported quantitatively with the reference block below. This is a consistency bound rather than an exact verification, because the closed form neglects the interface compliance ahead of the crack tip and the two-dimensional arm deformation that the finite-element model resolves; the computed loads are therefore expected to fall below it by an amount that grows with the process-zone length, and that expectation is itself testable. A quantitative comparison with the closed-form beam-on-cohesive-foundation solutions of Williams and Hadavinia [21] for the linear law is reported in Section 7.2.

The comparison is restricted to monotonic Mode-I loading. The present UEL evaluates the monotonic envelope and is not intended to represent cyclic unloading, reloading, or fatigue degradation.

4. Parametric Campaign

The campaign contains 100 unique simulations, summarized in Table 2.

Table 2. The 100-case campaign; the baseline case ($T_{\max} = 50$ MPa, $G_c = 0.100$ N/mm, $h = 1.6$ mm, $K_0 = 10^8$ N/mm^3) is shared by the three sweeps and counted once. The five checks below the total are not part of the campaign and are not used in any fit (Sections 7 and 7.3).

Component	Fixed values	Varied values	Cases
Strength	$h = 1.6$ mm, $G_c = 0.100$ N/mm, $K_0 = 10^8$ N/mm^3	$T_{\max} = 40, 50, 75, 100,$ and 125 Mpa six laws	30
Energy additions	$h = 1.6$ mm, $T_{\max} = 50$ MPa, $K_0 = 10^8$ N/mm^3	$G_c = 0.050, 0.075, 0.150,$ and 0.200 N/mm; six laws	24
Height additions	$T_{\max} = 50$ MPa, $G_c = 0.100$ N/mm, $K_0 = 10^8$ N/mm^3	$h = 3.2, 4.8, 6.4, 9.6, 14.4, 22.4,$ and 32.0 mm; six laws	42
Penalty checks	$h = 1.6$ mm, $T_{\max} = 50$ MPa, $G_c = 0.100$ N/mm	LIN and EXP at $K_0 = 10^7$ and 10^9 N/mm^3	4
	Total		**100**
Fixed-η checks (Section 7.3)	$T_{\max} = 50$ MPa, $G_c = 0.100$ N/mm, $K_0 = 10^8$ N/mm^3, $\eta = a_0/h = 18.75$	$h = 3.2$ mm, $a_0 = 60$ mm: REC, LIN, EXP; $h = 6.4$ mm, $a_0 = 120$ mm: LIN	4
Linear-geometry check (Section 7)	Baseline case ($h = 1.6$ mm, $a_0 = 30$ mm), geometric nonlinearity off	LIN	1

The baseline $T_{\max} = 50MPa$, $G_c = 0.100N/mm$, $h = 1.6mm$, and $K_0 = 10^8\ N/mm^3$ cases are shared by the strength, energy, and height comparisons and are counted only once in the total. Throughout this paper *baseline* denotes this shared $h = 1.6mm$ configuration, which anchors the one-factor sweeps and the normalizations of Eq. (18), whereas *reference block* denotes the complete six-law set at $h = 3.2mm$, which is used to display the local fields because its longer process zones are more finely resolved relative to the interface-element pitch. All 100 analyses bracketed the prescribed onset event, so no fitted point or complete parameter block required extrapolation or substitution.

Expressed in the groups of Eq. (2), the campaign covers $\Lambda = 0.137 - 5.495$, a span of a factor of 40, with the three sweeps occupying overlapping but distinct windows: $\Lambda = 0.13 - 2.7477$ (geometric mean 0.555) for the height sweep, 0.440–4.293 (geometric mean 1.342) for the strength sweep, and 1.374–5.495 (geometric mean 2.813) for the energy sweep. The strain-magnitude group τ spans 3.6×10^{-4}–1.1×10^{-3}. The strength and energy sweeps were both run at $h = 1.6mm$ and therefore hold $\eta = 18.75$ and $\kappa = 1456$ fixed, so within each of them Λ is varied in isolation, apart from τ in the strength sweep.

The height sweep necessarily varies all three of Λ, η, and κ at once, because the initial crack length was held at $a_0 = 30mm$. Over $h = 1.6mm - 32.0mm$ the crack-length ratio $\eta = a_0/h$ accordingly falls from 18.75 to 0.938 and κ rises from 1456 to 29120. The upper two heights, $h = 22.4mm$ and $32.0mm$, give $\eta = 1.34$ and 0.938 and are therefore no longer slender cracked beams; they are better described as short, deep bonded blocks. They are retained because the purpose of the height sweep is to traverse the beam-to-bulk crossover rather than to remain within beam theory, and because they supply the small-Λ end of the campaign. The fitted height exponents q_j should nevertheless be read as effective exponents for the combined variation of the three groups, not as partial derivatives at fixed η and κ; this qualification is carried through the analysis in Section 7.1. To separate the effect of Λ from that of η, four extra analyses outside the 100-case campaign were run with a longer precrack that keeps $\eta = 18.75$: three at $h = 3.2mm$ with $a_0 = 60mm$, and one for the linear law at $h = 6.4mm$ with $a_0 = 120mm$. They are reported in Section 7.3.

5. Debonding-Onset Definition and Extraction of the Process-Zone Length

The full opening of the bonded interface is calculated from the duplicated interface nodes:

$$\delta(x) = U_2^{\text{top}}(x) - U_2^{\text{bottom}}(x). \tag{10}$$

Debonding onset is defined by the opening at the original crack tip, $\delta(x = 0)$, reaching:

$$\delta(x = 0) = 0.999\,\delta_f. \tag{11}$$

This is a law-specific opening, not a common one, and the distinction is central to the comparison. Because δ_f is set by Eq. (7), it differs by a factor of 5.2 between the rectangular and finite exponential laws at the same G_c and $T_{\max}$. Aligning the six analyses on a common absolute opening would therefore compare interfaces at different states of damage, with some laws far from failure and others already past it, and any resulting spread in L_0 would be an artifact of the alignment rather than of the law. Aligning them instead on $\delta(x = 0)/\delta_f = 0.999$ compares them at the same normalized opening near failure at the original crack tip (checked at a node rather than at the first integration point), which is the event a mesh-design or propagation-criterion user actually needs to resolve. Note that the laws are compared at the same fraction of the final separation, not at the same traction, damage, or dissipated work: at $\delta = 0.999\,\delta_f$ the rectangular law still carries almost $T_{\max}$ at the tip, while the finite exponential law carries almost nothing. This remaining traction adds interface compliance ahead of the tip and sets the onset-load order discussed with Table 3. The comparison is thus of the spatial extent of the process zone at the same prescribed normalized-opening event in each analysis. That this choice does not drive the reported spreads is checked directly by moving the threshold about its baseline value of 0.999 from $0.99\delta_f$ to $0.9999\delta_f$, which changes the lengths by at most 4.11% and leaves the law ordering unchanged.

The onset frame is not taken as the increment at which the analysis was stopped, because a job may terminate several increments after the physical threshold has been exceeded. Instead, for each analysis, the saved frames are searched for the first bracket $(n-1, n)$ satisfying:

$$\delta_{n-1}(x = 0) < 0.999\delta_f \le \delta_n(x = 0). \tag{12}$$

The interpolation factor is:

$$\alpha = \frac{0.999\delta_f - \delta_{n-1}(x = 0)}{\delta_n(x = 0) - \delta_{n-1}(x = 0)}, \tag{13}$$

and every interface opening, applied displacement, reaction force, and step time is interpolated with the same α. This gives a common physical event even for jobs terminated several increments after onset. The load of Eq. (9) at the interpolated onset event is denoted P_0.

Table 3. Reference six-law results at interpolated debonding onset.

Law	L_0 (mm)	L_0/h	Onset load (N/mm)	Opening (mm)	C_{shape}
REC	0.898	0.281	5.130	0.422	0.259
LIN	1.473	0.460	5.053	0.435	0.425
TRAP	1.094	0.342	5.108	0.426	0.316
EXP	3.069	0.959	4.839	0.475	0.886
POLY	2.000	0.625	4.976	0.449	0.577
MULTI	2.567	0.802	4.909	0.461	0.741

Table 4. Fitted power-law exponents; least-squares 95% intervals in brackets. Five points per law for the strength and energy fits, eight for the height fits.

Law	Strength m_j	Energy n_j	Height q_j
REC	-1.251 $[-1.428, -1.074]$	0.534 $[0.491, 0.578]$	0.285 $[0.232, 0.339]$
LIN	-1.136 $[-1.316, -0.957]$	0.445 $[0.394, 0.496]$	0.331 $[0.273, 0.390]$
TRAP	-1.204 $[-1.344, -1.065]$	0.537 $[0.500, 0.573]$	0.283 $[0.220, 0.347]$
EXP	-0.900 $[-1.003, -0.797]$	0.374 $[0.364, 0.384]$	0.502 $[0.469, 0.534]$
POLY	-1.042 $[-1.199, -0.885]$	0.446 $[0.366, 0.525]$	0.394 $[0.346, 0.442]$
MULTI	-0.969 $[-1.072, -0.866]$	0.396 $[0.388, 0.404]$	0.457 $[0.419, 0.495]$

For each saved frame, the duplicated upper and lower interface nodes are paired by their common x-coordinate and ordered from the original crack tip into the bonded region. Equation (10) gives the nodal opening profile. The two profiles surrounding onset are first interpolated in time using the same α from Eq. (13); therefore, the global response and every local interface opening correspond to the same interpolated event.

On this interpolated profile, the failure front x_f is the crossing of $\delta = 0.999\delta_f$, while the damage front x_d is the crossing of $\delta = \delta_0 = T_{\max}/K_0$. Each crossing is located by linear spatial interpolation between the two adjacent interface nodes that bracket its threshold. Consequently, the reported front locations are not restricted to multiples of the 0.025 mm interface-element length. The onset cohesive-zone length, denoted L_0 elsewhere in this paper, is:

$$L_{\text{cz}}^{\text{onset}} \equiv L_0 = x_d - x_f = x(\delta = \delta_0) - x(\delta = 0.999\delta_f). \tag{14}$$

At first debonding, the failure front is at the original crack tip to within the temporal and spatial interpolation tolerances, so $x_f \approx 0$ and $L_0 \approx x_d$. A positive value is accepted only when both crossings are bracketed inside the bonded interface. This procedure is applied independently to all 100 analyses and also provides the number of resolved cohesive elements, $L_0/\Delta x$, as a mesh-resolution check.

For every analysis, the following quantities were determined at the interpolated onset event: the onset-frame bracket and interpolation factor; L_0, L_0/h, the intrinsic length $E'G_{\text{c}}/T_{\max}^2$, the beam scaling length, and C_{shape}; the onset load, applied opening, and peak load up to onset; the load–opening history up to onset; and the onset profiles of opening, reconstructed normal traction, secant damage, and accumulated cohesive work.

6. Analysis Methods

For each law, the strength sweep is fitted as:

$$L_0 = a_j T_{\max}^{m_j}, \tag{15}$$

the energy sweep as:

$$L_0 = b_j G_{\text{c}}^{n_j}, \tag{16}$$

and the fixed-a_0 height sweep as:

$$L_0 = d_j h^{q_j}, \tag{17}$$

where a_j, b_j, and d_j are law-specific prefactors, distinct from the normalized post-peak area A_j of Eq. (6). The beam scaling predicts $m_j = -0.5$, $n_j = 0.25$, and $q_j = 0.75$. All powers are obtained by ordinary least squares in log–log space and are reported with conventional least-squares 95% intervals; the range of the corresponding coefficients of determination is quoted with the fits. A nested-model F-ratio compares a reduced model with six law-specific intercepts and one shared slope against a model with six law-specific intercepts and slopes. A common exponent requires both a high within-law fit quality and a small loss of fit in the reduced model. Only cases that bracket the prescribed onset event are included; cross-law spreads and common-range fits use complete six-law blocks.

The statistical status of these intervals and fit comparisons requires a comment, because the underlying data are deterministic: repeating a simulation returns the same L_0 to machine precision, so there is no sampling distribution in the usual sense. The residuals about each log–log fit therefore measure systematic departure from a pure power law—that is, the curvature of F_j discussed in Section 7.1—together with the finite resolution of the onset extraction, and not experimental noise. The intervals and F-ratios are accordingly used as calibrated measures of lack of fit: they show whether the six laws depart from a shared slope more than each law departs from its own straight line. The intervals in Table 4 should be read in this way, not as sampling uncertainty. The adjacent-point slopes of Section 7.1 check the same question without any regression. The threshold and penalty checks are sensitivity checks only; they do not give error bounds for the exponents or a mesh-convergence estimate. Degrees of freedom follow the block structure: the strength and energy fits use five levels for each of six laws, giving $F(5{,}18)$ for the shared-slope comparison, and the height fits use eight levels for each of six laws, giving $F(5{,}36)$.

For compact comparison within the sampled one-factor ranges, the three fits can also be written relative to the law-specific baseline as:

$$\frac{L_0^{(j)}}{L_{0,\text{base}}^{(j)}}=\left(\frac{T_{\max}}{T_{\max,\text{base}}}\right)^{m_j}\left(\frac{G_\text{c}}{G_{\text{c,base}}}\right)^{n_j}\left(\frac{h}{h_\text{base}}\right)^{q_j}. \tag{18}$$

This separable expression summarizes the one-factor sweeps; interactions were not sampled and are therefore not implied. For every physical case, the shape coefficient $C_{\text{shape},j}\equiv C_j$ of Eq. (1):

$$C_{\text{shape},j}=\frac{L_0}{(E'G_\text{c}/T_{\max}^2)^{1/4}h^{3/4}} \tag{19}$$

is calculated. Its coefficient of variation within each sweep quantifies transferability. Systematic drift with h indicates that a single beam-regime coefficient is insufficient over the sampled range and that the finite-geometry dependence in Eq. (2) cannot be absorbed into a law-specific constant.

For every complete six-law parameter block, global and local shape sensitivities are defined relative to the linear law:

$$S_P=100\frac{P_0^{\max}-P_0^{\min}}{P_0^{\text{LIN}}},\qquad S_L=100\frac{L_0^{\max}-L_0^{\min}}{L_0^{\text{LIN}}}. \tag{20}$$

Here P_0 denotes the load per unit width of Eq. (9) evaluated at the interpolated onset event of Eq. (11), and the maxima and minima are taken over the six laws of a block. The comparison of S_L and S_P tests whether global near-equivalence can coexist with local non-equivalence.

7. Results

All 100 analyses produced a valid onset bracket, an interpolation factor between zero and one, and a positive L_0. The extracted lengths ranged from 0.200 mm to 9.074 mm, corresponding to approximately 8–363 interface elements. Even the shortest process zone in the campaign is therefore resolved by eight interface elements at the fixed pitch $\Delta x=0.025mm$, which exceeds the minimum of about three elements commonly recommended for cohesive-zone resolution [28, 29], and every other case resolves its own process zone with correspondingly more elements. The three-element figure is a practical rule rather than a sharp threshold, and Turon et al. note that the minimum number of elements needed in the cohesive zone is not well established [28]. It was also derived for steady-state propagation with a bilinear law, whereas the quantity extracted here is the active zone at first debonding. With these caveats in mind, eight elements, more than twice the usual floor, was considered sufficient, and no separate mesh-refinement study of L_0 was carried out. The shortest zones ($L_0=0.200mm$, eight elements) are nonetheless the ones with the smallest margin. Three observations support this choice, although they are not a formal convergence study. First, the fronts are located by interpolation between nodes (Section 5), so L_0 is not tied to multiples of the element length, and moving both fronts through the threshold check below changes L_0 by at most 4.11%. Second, along the strength sweep the rectangular law is resolved by 8 to 33 elements and the linear law by 14 to 53, and the adjacent-point slopes of Section 7.1 keep rising toward the coarsely resolved end, as the crossover trend predicts, with no reversal there. Third, the linear-law onset loads at the coarse end match the closed-form solution of Section 7.2 about as well as those at the fine end (0.9% against 0.5%); this check does not reach the very shortest zone, because the elastic–linear branch does not exist at $T_{\max}=125MPa$. The pitch is identical across all six laws in every block, so no law benefits from a finer mesh than another, although each law resolves its zone with a different number of elements. Three of the 100 analyses—the finite exponential law at $T_{\max}=100$ and $125MPa$ and the trapezoidal law at $125MPa$, all at $h=1.6mm$—did not converge without stabilization and were rerun with Newton line search and adaptive automatic stabilization (initial dissipated-energy fraction 2×10^{-4}, accuracy tolerance 0.01); the other 97 used none. Because artificial viscosity can lengthen the apparent process zone, the ratio of stabilization to internal energy was extracted for each of these runs at the last saved frame, just past onset (crack-tip openings of 1.19, 1.01, and 1.04δ_f, that is 19%, 1%, and 4% beyond the final separation): ALLSD/ALLIE = 1.0×10^{-7}, 2.0×10^{-6}, and 3.5×10^{-7}. These are post-onset values rather than values at onset, and ALLIE does not include the energy of the user elements, whose energy array is not populated in the present implementation. At five to seven orders of magnitude below unity, they suggest that stabilization had a negligible effect, and the three results are retained; they are the only stabilized points in the campaign. A rerun of the baseline linear-law case with geometric nonlinearity switched off changed the onset load by −0.09% and the applied opening at onset by +0.10%, and lengthened L_0 by 4.4% (1.050 mm to 1.096 mm)—the size of the onset-threshold sensitivity, and about thirty times smaller than the law-to-law spread of the same block. Because the user element takes its rotation and integration length from the deformed configuration in both runs, this rerun measures the effect of the bulk setting only; it is not a separate measurement of the sensitivity to τ. The median saved-frame bracket width was $0.041\delta_f$; the interpolated event lay a median $0.0066\delta_f$, and at most $0.071\delta_f$, from the nearer stored frame.

Table 3 gives the complete reference block at $h=3.2mm$, $T_{\max}=50MPa$, $G_\text{c}=0.100N/mm$, and $K_0=10^8N/mm^3$. The global onset-load spread is 5.77% of the linear-law onset load, whereas the local L_0 spread is 147.41% of the linear-law length. The load–opening curves remain closely grouped through most of the pre-onset response, while the local opening, traction, and cohesive-work profiles occupy markedly different distances ahead of the crack tip (Figs. 3 and 4).

A simple analytical bound corroborates the onset loads in Table 3. For the reference block, linear-elastic simple-beam theory with built-in arms gives $P_\text{LEFM}=\sqrt{E'G_\text{c}h^3/(12a_0^2)}=5.77N/mm$ at $G=G_\text{c}$. All six computed onset loads lie at 84–89% of this bound, and the deficit grows monotonically with L_0: laws with longer process zones (MULTI, EXP) introduce more interface compliance ahead of the crack tip and therefore reach the common onset event at a lower load [21, 26]. One caveat applies. Because all six laws share G_c, the LEFM limit does not depend on shape, so the global spread must shrink as $\Lambda\rightarrow 0$ whatever the local behaviour. The small onset-load spread is thus partly built into the design; the more useful global result is the 11–16% drop below the beam value and its link to L_0. Section 7.2 replaces this bound with a direct prediction for the linear law. The global responses are thus mutually consistent and physically bounded, while remaining far less discriminating than the local lengths.

The same length ordering, REC < TRAP < LIN < POLY < MULTI < EXP, occurred in all 16 complete six-law blocks. Averaged over these blocks, the lengths normalized by the linear law were 0.595, 0.716, 1.000, 1.402, 1.808, and 2.221, respectively. In contrast, the corresponding mean onset loads normalized by the linear law were 1.013, 1.010, 1.000, 0.985, 0.970, and 0.954. Thus, the law ranking is strong locally but compressed globally.

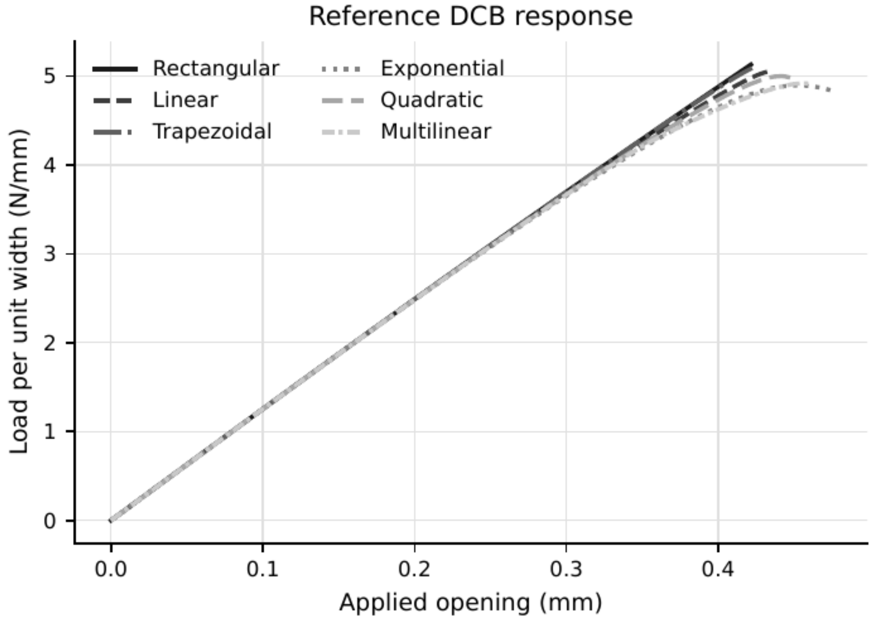

Fig. 3. Load–opening curves for the complete $h = 3.2mm$ reference block; the curves stay close up to onset.

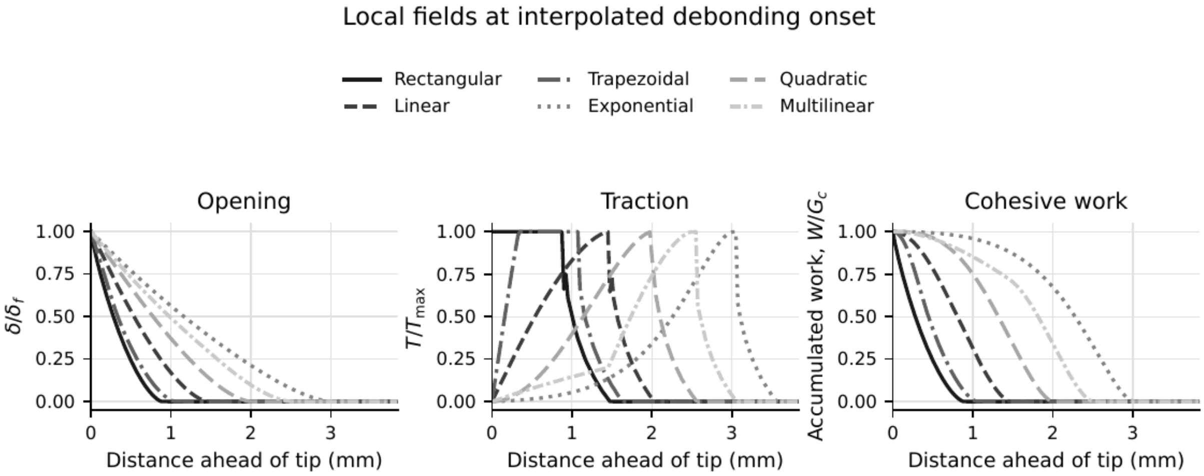

Fig. 4. Onset profiles of opening, traction, and cohesive work for the reference block; the process zones differ markedly in length.

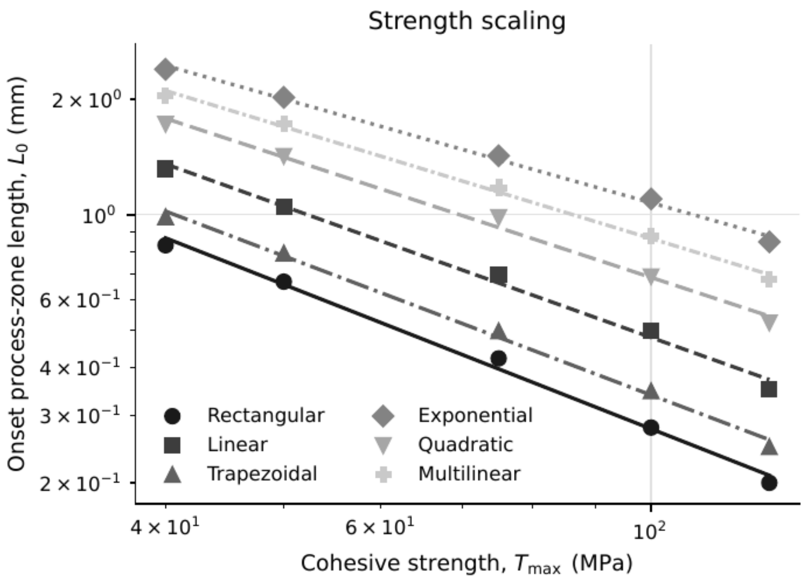

Fig. 5. Process-zone length versus cohesive strength for each law. Symbols: finite-element results; lines: log–log least-squares fits, which need not pass through every point.

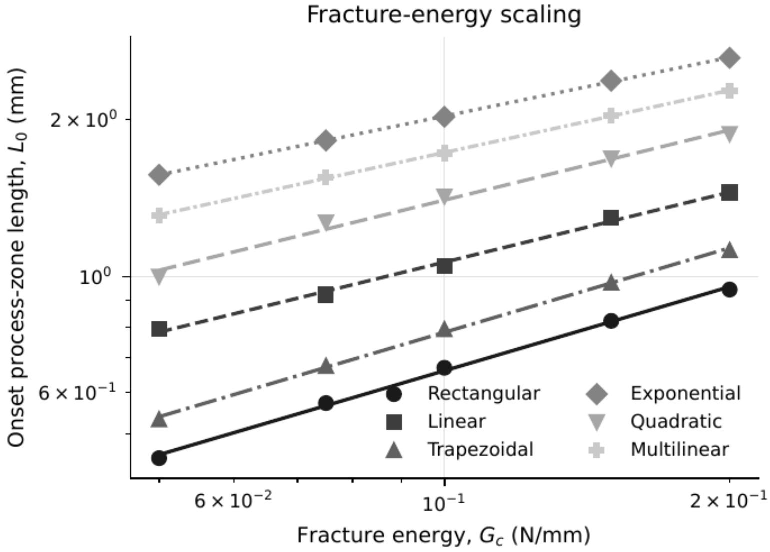

Fig. 6. Process-zone length versus fracture energy for each law (five levels). Symbols: finite-element results; lines: log–log least-squares fits.

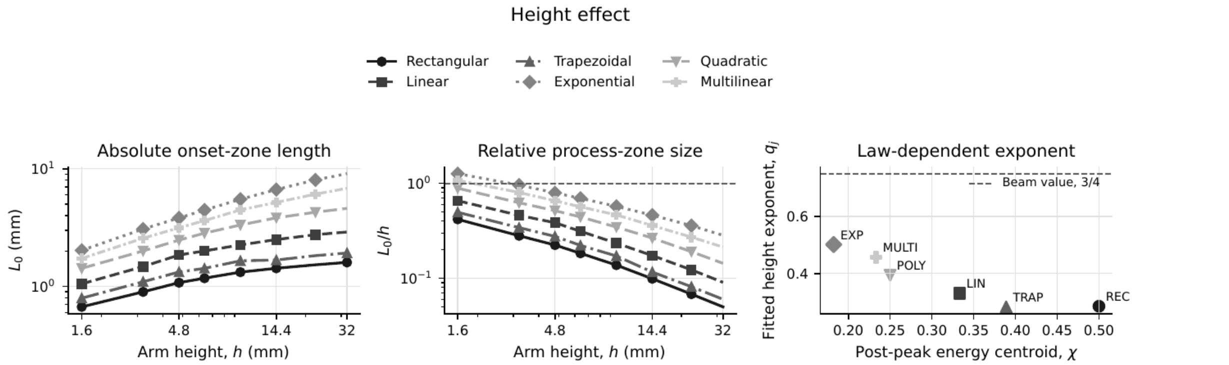

Fig. 7. Absolute and normalized process-zone length versus arm height, and the fitted height exponent of each law (eight heights, 1.6–32.0 mm).

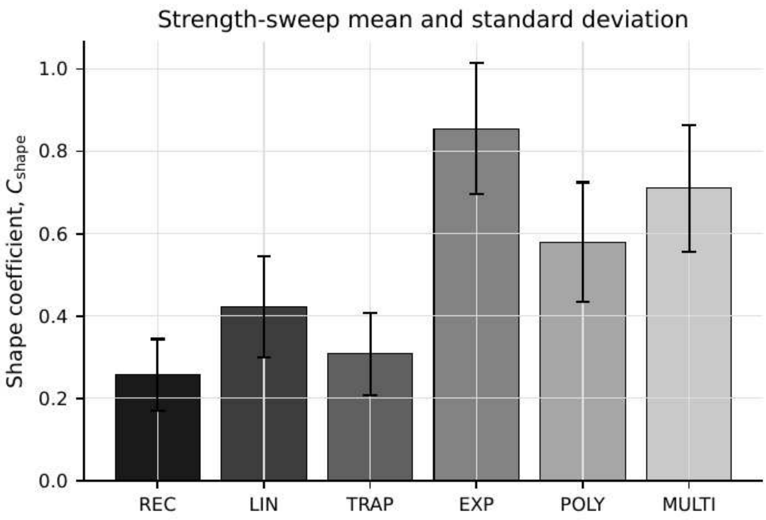

Fig. 8. Mean beam shape coefficient over the strength sweep; error bars show one standard deviation.

The law-specific exponents and least-squares 95% intervals are summarized in Table 4. All individual log–log fits were strong ($R^2 = 0.927 - 1000$), but their slopes were not common. The strength exponents ranged from -1.251 to -0.900, the energy exponents from 0.374 to 0.537, and the effective height exponents from 0.283 to 0.502. All point estimates therefore differed substantially from the coefficient-only beam values -0.5, 0.25, and 0.75. The underlying log–log data and fits are plotted for the strength, energy, and height sweeps in Figs. 5, 6, and 7, respectively.

Imposing one shared exponent produces a large loss of fit relative to law-specific slopes: strength gave $F(5,18) = 8.87$; fracture energy gave $F(5,18) = 22.90$; and height gave $F(5,36) = 12.59$. Each ratio compares the extra residual caused by forcing one shared slope with the residual of the law-specific fits. The shared-slope residual is 3.46, 7.36, and 2.75 times the law-specific residual for the three sweeps.

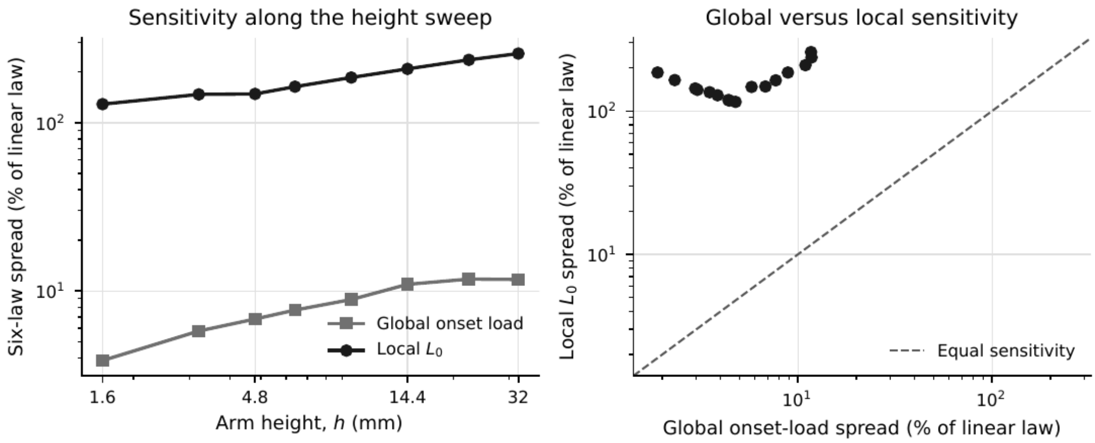

Fig. 9. Six-law sensitivity along the height sweep, and global versus local sensitivity for all 16 blocks.

The height sweep also invalidated a transferable C_{shape}. Across the eight complete heights its coefficient of variation was 24.3–44.0%, depending on law, and its value at $h = 32.0mm$ was only 0.253–0.474 of the corresponding $h = 1.6mm$ value. The coefficient therefore drifted systematically rather than fluctuating about a law-specific constant. The strength sweep gives the same conclusion from a second direction: within-law coefficients of variation were 18.6–34.1% (Fig. 8).

Across the 16 complete six-law blocks, S_P ranged from 1.89% to 11.75%, whereas S_L ranged from 115.87% to 257.91%. The ratio S_L/S_P was 19.1–98.2, so every complete block lies far above the equal-sensitivity line in Fig. 9. Along the height sweep, both sensitivities increased, but the local spread remained dominant.

Changing K_0 from 10^7 to $10^9\ N/mm^3$ changed L_0 by 0.15% for LIN and 0.74% for EXP, normalized by their baseline values. Changing the onset threshold from $0.99\delta_f$ to $0.9999\delta_f$ about the baseline value 0.999 in the complete $h = 3.2mm$ block changed the law-specific lengths by at most 4.11% across that range (4.03% relative to the baseline value) and did not change their ordering. These variations are small relative to the six-law local spreads.

7.1. Regime interpretation of the law-dependent exponents

The exponents of Table 4 were fitted independently, but Eq. (2) implies that they are not independent quantities. If dependence on the other dimensionless groups is negligible and F_j is locally a power law in Λ over the window sampled by a given sweep, then $L_0 = hF_j(\Lambda)$ with $\Lambda = E'G_c/(T_{\max}^2 h)$ gives $m_j = -2s_j$, $n_j = s_j$, and $q_j = 1 - s_j$, where s_j is the local logarithmic slope defined in Eq. (3). Each sweep therefore yields a conditional, window-averaged estimate of the underlying slope function $s_j(\Lambda)$, evaluated over a different window, and the three estimates can be compared directly even though the raw exponents cannot. Table 5 reports the resulting values; the height estimates also include the effects of the other groups varying along that sweep.

Three consistency checks follow. First, all eighteen estimates fall inside the physically motivated bracket $[1/4,1]$, with none closer than 0.12 to either limit; the campaign therefore sits entirely in the crossover region between slender-beam and bulk cohesive behavior, which is the regime in which a single transferable exponent should not be expected to exist. Second, for every law the three estimates order as $s_{\text{height}} > s_{\text{strength}} > s_{\text{energy}}$, matching the inverse ordering of the geometric-mean Λ sampled by the three sweeps, $0.555 < 1.342 < 2.813$. This ordering is consistent with the limiting analysis: $s \to 1$ as $\Lambda \to 0$, where the process zone is short relative to the arm and the response is bulk-like, and $s \to 1/4$ as $\Lambda \to \infty$, where the arm is slender relative to the cohesive length. The three sweeps are thus not three conflicting measurements of one exponent but window-averaged views of one broad crossover trend in $s(\Lambda)$, within which the adjacent-pair slopes of Table 6 show local reversals. Third, the same statement appears in a form that involves no height data at all: because m_j is measured at smaller mean Λ than n_j, a concave $\ln F_j$ requires $|m_j/n_j| > 2$, and the measured ratios are 2.24–2.55 for all six laws.

The strength and energy sweeps provide the cleanest form of this test, since both were run at $h = 1.6mm$ and therefore share identical $\eta = 18.75$ and $\kappa = 1456$; the only group that differs between them is Λ, together with $\tau = T_{\max}/E'$ in the strength sweep. If τ exerted a first-order influence, the strength-sweep slopes would be displaced away from the trend defined by the energy sweep, which varies Λ at fixed $\tau = 4.55 \times 10^{-4}$. They are not: the two sets differ by only 0.065–0.123, always in the sign demanded by the Λ offset, and the scatter of that difference across laws is smaller than the law-to-law spread of s itself. The omission of τ from the argument list of F_j in Eq. (2) is therefore consistent with the data over the sampled range, as anticipated on the grounds that $\tau \lesssim 10^{-3}$ throughout. The strength sweep cannot vary τ independently of Λ, so this comparison is a null result against the τ-invariant energy sweep rather than a direct measurement of the τ sensitivity.

Table 5. Window-averaged logarithmic slope $s_j = \partial \ln F_j/\partial \ln \Lambda$ from each sweep, using $s = -m/2$, $s = n$, and $s = 1 - q$. The geometric-mean Λ of each sweep is given in the column heading; the slender-beam and bulk limits bound s between $1/4$ and 1.

	Height sweep	Strength sweep	Energy sweep		
Law	$\Lambda = 0.555$	$\Lambda = 1.342$	$\Lambda = 2.813$	$\lvert m_j/n_j \rvert$	A_j
REC	0.715	0.625	0.534	2.343	1.000
TRAP	0.717	0.602	0.537	2.242	0.750
LIN	0.669	0.568	0.445	2.553	0.500
POLY	0.606	0.521	0.446	2.336	0.333
MULTI	0.543	0.484	0.396	2.447	0.250
EXP	0.498	0.450	0.374	2.406	0.193

Table 6. Slopes $s_j = \partial \ln F_j / \partial \ln \Lambda$ between adjacent points of each sweep, without regression ($s = -m/2, n$ or $1-q$), listed in order of decreasing Λ. Height-sweep values follow the sampled path, along which η and κ also vary.

Sweep	Interval	REC	TRAP	LIN	POLY	MULTI	EXP
Strength (MPa)	40→50	0.490	0.489	0.509	0.430	0.387	0.378
	50→75	0.568	0.577	0.505	0.454	0.471	0.433
	75→100	0.722	0.624	0.582	0.617	0.508	0.450
	100→125	0.744	0.751	0.794	0.622	0.580	0.577
Energy (N/mm)	0.200→0.150	0.480	0.498	0.384	0.374	0.384	0.351
	0.150→0.100	0.510	0.506	0.523	0.415	0.408	0.393
	0.100→0.075	0.541	0.562	0.444	0.396	0.377	0.361
	0.075→0.050	0.599	0.582	0.373	0.589	0.406	0.374
Height (mm)	1.6→3.2	0.576	0.537	0.512	0.509	0.426	0.399
	3.2→4.8	0.556	0.526	0.442	0.475	0.499	0.463
	4.8→6.4	0.697	0.754	0.724	0.529	0.507	0.465
	6.4→9.6	0.707	0.637	0.710	0.606	0.485	0.478
	9.6→14.4	0.814	0.961	0.740	0.655	0.636	0.531
	14.4→22.4	0.846	0.807	0.784	0.751	0.637	0.573
	22.4→32.0	0.867	0.854	0.852	0.791	0.675	0.658

A quantitative version of the same check uses the spacing of the three windows. Treating the pairs of estimates as finite differences of s with respect to $\ln\Lambda$, the implied curvature $-\partial s/\partial \ln\Lambda$ is 0.054–0.130 between the height and strength windows and 0.088–0.166 between the strength and energy windows. The two intervals return the same order of magnitude for every law, so the eighteen estimates are compatible with a broad crossover interpretation for $F_j(\Lambda)$ per law without establishing a unique one-variable curve or pointwise concavity. The height sweep remains the least clean of the three, because η and κ vary along it as Λ does; its s should be read as an effective slope that may absorb some residual geometric dependence, and it is not used above to establish the τ argument.

The exponents in Table 4 are single straight-line fits through a curved function, so they depend on where the points lie, and part of the difference between laws could come from this curvature rather than from shape. Table 6 avoids the fit by giving slopes between adjacent points, converted to s as in Table 5. The slopes rise toward small Λ in every sweep (from 0.38–0.51 to 0.58–0.79 in the strength sweep, 0.35–0.50 to 0.37–0.60 in the energy sweep, and 0.40–0.58 to 0.66–0.87 in the height sweep), and for the thickest arms they come closer to the bulk limit $s = 1$ than any fitted value. The rise is not steady: 14 of the 72 successive pairs decrease (one in the strength sweep, five in the energy sweep, and eight in the height sweep), the largest drop being 0.961 to 0.807 for the trapezoidal law between $h = 9.6$–$14.4mm$ and 14.4–$22.4mm$. Table 6 therefore supports a broad crossover trend rather than a smooth concave curve, and these local drops may partly reflect the resolution of the onset extraction. The finite exponential law has the lowest s in 13 of the 15 intervals, and the two laws with the largest post-peak area (rectangular and trapezoidal) stay above the two with the smallest (multilinear and finite exponential) in all 15. The linear and quadratic laws ($A_j = 0.500$ and 0.333) change places with each other and with their neighbours; for example, the linear law falls below the finite exponential law in the 0.050–0.075 N/mm interval and below the multilinear and quadratic laws in the 3.2–4.8 mm interval. For four of the five neighbouring pairs in the A_j order, the sign of the difference changes between intervals; only the multilinear–exponential pair keeps its order. The law effect therefore survives without regression as a clear separation of the extreme laws, while the finer ordering in Table 4 should not be over-read.

The law dependence itself is also systematic rather than arbitrary. The window-averaged slope s_j increases monotonically with the normalized post-peak area A_j in the strength sweep (Spearman $\rho = +1.000$) and near-monotonically in the height and energy sweeps ($\rho = +0.943$ and $+0.886$); because χ_j is rank-identical to A_j across the six laws, the same coefficients apply to the centroid. Laws with blunt, area-rich post-peak branches behave more bulk-like over the sampled ranges of Λ, whereas the finite exponential law, whose traction collapses fastest after the peak, sits closest to the slender-beam limit. Shape therefore does not shift a common curve vertically, as a multiplicative C_{shape} would require; it shifts the specimen along the crossover, which is why no single coefficient transfers.

7.2. Comparison with closed-form beam-on-cohesive-foundation solutions

Williams and Hadavinia [21] give closed-form solutions for an elastic arm on a cohesive foundation. Two are used here: a rigid–linear softening law (their linear damage form) and the same law combined with the through-thickness compliance of the arm, given by the Kanninen foundation stiffness $2E'/h$ (their elastic–linear damage form). Their model is a single cantilever, so the symmetric DCB must first be mapped onto it. By symmetry, each arm deflects $v = \delta/2$ while carrying the full traction T, so the arm sees a law with the same peak $T_{\max}$ but an area $\int T\, dv = G_c/2$. In the purely elastic limit, the single-arm solution gives the foundation length $D = h/6^{1/4} = 0.639h$, the known end correction of the isotropic DCB, which confirms this mapping (D is the analytical foundation length, not the applied opening Δ of Eq. (9)). The characteristic length is then $D^4 = (2/3)E'(G_c/2)h^3/T_{max}^2$, and the elastic–linear solution exists only when $6(D/h)^4 = 2\Lambda$ exceeds one, that is, for $\Lambda > 1/2$. The ratio δ_0/δ_0 is 1.25×10^{-4} at the baseline and at most 5×10^{-4} where that solution exists (7.8×10^{-4} at $T_{max} = 125MPa$, where it does not), so the present linear law is rigid–linear for practical purposes. The solutions were evaluated with E', $a_0 = 30mm$, and the first root of the eigen-equations at finite crack length; they also give the correction $\psi = G_c/G_b$ to simple-beam theory, so that the onset load is $P_0 = P_{LEFM}/\sqrt{\psi}$. Table 7 compares these predictions with the finite-element results for the linear law.

The onset load is matched closely wherever the elastic–linear solution exists. For the eight $h = 1.6mm$ cases, the finite-element load is 0.43–0.90% below the prediction; at $h = 3.2, 4.8$, and $6.4mm$ it is 4.82%, 4.03%, and 4.12% below. The other five cases in Table 7, including $T_{max} = 125MPa$ at $h = 1.6mm$, have no elastic–linear prediction. The finite-element load is always the lower one, as expected, and the gap is larger for the thicker arms. Possible causes are transverse shear, which an Euler–Bernoulli arm ignores, the two-dimensional stress state near the tip, and the approximate treatment of root rotation in the analytical model; these were not separated from the effects of front definition and mesh. The comparison is therefore a consistency check on the onset load; it does not by itself verify the energy balance of the element or the convergence of the extracted length.

Table 7. Linear-law finite-element results versus the closed-form solutions of Williams and Hadavinia [21] (single-arm energy $G_c/2, a_0 = 30mm$). P_{LEFM} is the simple-beam value of Section 3. A dash marks cases with no elastic–linear solution ($\Lambda < 1/2$). Values are rounded; percentages in the text use unrounded values.

Case	Λ	L_0 FE (mm)	ℓ rigid–linear (mm)	ℓ elastic–linear (mm)	P_0 FE (N/mm)	P elastic–linear (N/mm)	P_{LEFM} (N/mm)
$h = 1.6,\ T_{\max} = 40$	4.293	1.318	2.347	1.215	1.920	1.930	2.041
$h = 1.6,\ T_{\max} = 50$ (baseline)	2.747	1.050	2.097	0.935	1.930	1.941	2.041
$h = 1.6,\ T_{\max} = 75$	1.221	0.697	1.709	0.471	1.944	1.958	2.041
$h = 1.6,\ T_{\max} = 100$	0.687	0.499	1.478	0.165	1.951	1.969	2.041
$h = 1.6,\ T_{\max} = 125$	0.440	0.350	1.321	—	1.957	—	2.041
$h = 1.6,\ G_c = 0.050$	1.374	0.794	1.760	0.536	1.373	1.383	1.444
$h = 1.6,\ G_c = 0.075$	2.060	0.924	1.950	0.765	1.675	1.687	1.768
$h = 1.6,\ G_c = 0.150$	4.121	1.298	2.323	1.188	2.354	2.365	2.500
$h = 1.6,\ G_c = 0.200$	5.495	1.450	2.498	1.380	2.709	2.721	2.887
$h = 3.2$ (reference block)	1.374	1.473	3.549	1.089	5.053	5.308	5.774
$h = 4.8$	0.916	1.847	4.837	0.980	9.095	9.477	10.608
$h = 6.4$	0.687	2.000	6.031	0.692	13.638	14.225	16.332
$h = 9.6$	0.458	2.249	8.242	—	23.711	—	30.004
$h = 14.4$	0.305	2.499	11.289	—	40.127	—	55.120
$h = 22.4$	0.196	2.749	15.943	—	68.711	—	106.940
$h = 32.0$	0.137	2.899	21.108	—	102.718	—	182.596

Table 8. Fixed-η runs ($\eta = 18.75$) compared with the fixed-a_0 sweep at the same heights and with the $h = 1.6mm$ baseline. P_0/P_{LEFM} is the onset load divided by the simple-beam value.

Law	h (mm)	a_0 (mm)	η	Λ	L_0 (mm)	L_0/h	P_0 (N/mm)	P_0/P_{LEFM}	C_{shape}
REC	1.6	30	18.75	2.747	0.669	0.418	1.951	0.956	0.325
REC	3.2	30	9.375	1.374	0.898	0.281	5.130	0.889	0.259
REC	3.2	60	18.75	1.374	0.880	0.275	2.665	0.923	0.254
LIN	1.6	30	18.75	2.747	1.050	0.656	1.930	0.945	0.510
LIN	3.2	30	9.375	1.374	1.473	0.460	5.053	0.875	0.425
LIN	3.2	60	18.75	1.374	1.473	0.460	2.644	0.916	0.425
LIN	6.4	30	4.688	0.687	2.000	0.312	13.638	0.835	0.343
LIN	6.4	120	18.75	0.687	1.924	0.301	3.853	0.944	0.330
EXP	1.6	30	18.75	2.747	2.024	1.265	1.877	0.919	0.982
EXP	3.2	30	9.375	1.374	3.069	0.959	4.839	0.838	0.886
EXP	3.2	60	18.75	1.374	3.014	0.942	2.586	0.896	0.870

The process-zone length is predicted much less accurately, which is itself informative. The rigid–linear solution, which ignores arm compliance, overestimates L_0 by factors of 1.7 to 7.3. The elastic–linear solution underestimates it, by 5% at Λ = 5.50 and by up to about a factor of three at Λ = 0.69, although not as a single function of Λ: the two cases with Λ = 1.374 are underestimated by 33% and 26%. It has no solution for the five cases with the lowest Λ. Part of the gap comes from how the zone is defined: here the length ends where $\delta = \delta_0$, whereas the rigid–linear model ends its damaged region where opening, slope, and curvature vanish, and the elastic–linear model joins a still-deforming elastic foundation at a non-zero displacement. The two-dimensional arm deformation, which a beam model does not capture, may also contribute. The analytical comparison thus shows the same pattern as the rest of the paper: where the elastic–linear solution exists, the global onset load is matched within 1% at h = 1.6 mm and 5% at h = 3.2–6.4 mm, while the local zone length is predicted only to within a factor of order one. The shear-corrected Timoshenko model of [26] is the natural next step for the length.

7.3. Fixed-η height check

Along the height sweep, η falls from 18.75 to 0.94 and κ rises by a factor of 20 while Λ falls, so the drift of C_{shape} and the height exponents in Table 4 mix all three effects. The three extra analyses at h = 3.2 mm and a_0 = 60 mm (Section 4) use the campaign mesh with a longer traction-free precrack and the same interface mesh. They keep η = 18.75, as in the h = 1.6 mm baseline, while Λ = 1.374 and κ = 2912 keep their h = 3.2 mm values. A fourth analysis, for the linear law at h = 6.4 mm and a_0 = 120 mm, extends this line. Comparing these runs with the fixed-a_0 results at the same height isolates the effect of η at fixed Λ and κ (Table 8). Doubling η changed L_0 by –2.0%, +0.02%, and –1.8% for the rectangular, linear, and finite exponential laws, and quadrupling it changed the linear-law length at h = 6.4 mm by –3.8%. C_{shape} changed only from 0.259 to 0.254, 0.425 to 0.425, and 0.886 to 0.870, so almost all of its drift between h = 1.6 mm and 3.2 mm (0.325 → 0.254, 0.510 → 0.425, 0.982 → 0.870) remains at fixed η. The fixed-η slopes between h = 1.6 and 3.2 mm are s = 0.605, 0.511, and 0.425, compared with 0.576, 0.512, and 0.399 at fixed a_0; for the linear law between 3.2 and 6.4 mm they are 0.615 and 0.559. The differences (0.03 or less below 3.2 mm and 0.056 above) are similar to the interval-to-interval scatter in Table 6, and the law order is unchanged. For the laws and heights checked, η therefore changes L_0 by only a few percent, and the drift of C_{shape} comes from Λ and κ rather than from η. These four runs do not cover the two deepest cases or three of the laws, and κ still changes with height, so the height exponents remain effective exponents along the sampled path. A few percent in L_0 can still be about ten percent in a slope (0.056 against 0.559). The onset load, in contrast, does depend on η: relative to the simple-beam value it rises from 0.84–0.89 to 0.90–0.94 when a_0 is doubled or quadrupled, as predicted by the $(1 + D/a)^2$ correction of [21].

8. Discussion

The central result is the systematic separation between global and local sensitivity. Matching K_0, $T_{\max}$, and G_c constrained the pre-onset structural response, yet it did not constrain the spatial distribution of traction and work within the interface. Thus, agreement in a DCB load–opening curve is not sufficient evidence that two cohesive laws predict equivalent process-zone fields. This extends earlier observations of global–local divergence in narrower law comparisons [19] by showing the same behavior across six laws and three independent parameter sweeps. It also provides a controlled explanation for the non-unique parameters obtained from global DCB data [33] and reinforces the value of crack-tip or full-field measurements for local identification [34–36].

The invariant ordering of L_0 offers a mechanistic interpretation of the shape effect. Along the sequence REC, TRAP, LIN, POLY, MULTI, and EXP, the normalized post-peak area A_j and energy centroid χ_j decrease, while the final separation δ_f required to preserve G_c increases. This combination coincides with a progressively longer active zone and explains why equal strength and total work do not imply equal spatial dissipation. The ordering is robust within the present design, but it should not be interpreted as proof that χ_j is a unique shape parameter: A_j, χ_j, and δ_f co-vary among the selected laws, so their individual causal effects cannot be separated here. In addition, the six laws do not differ in shape alone. Keeping G_c, $T_{\max}$, and K_0 fixed forces δ_f to change by a factor of 5.2 across the set (Eq. (7)), so "shape" here means the combined change of the post-peak curve, the final separation, and how the dissipated work is spread along the separation. Within this family these cannot be separated, since fixing δ_f would change G_c; all results should be read as the effect of this combined change, even though other laws of equal area could share a final separation. The area A_j is a convenient single measure of it because Eq. (7) makes δ_f a function of A_j.

The scaling analysis moves the conclusion beyond a simple ranking of laws. If shape acted only through a multiplicative coefficient, the log–log responses would remain parallel. Instead, the shared-slope models fitted markedly worse for the strength, energy, and height sweeps, and C_{shape} decreased systematically with height. Law shape therefore interacts with the sampled material and geometric parameters, changing the fitted exponents as well as the prefactor. Equation (18) should consequently be used only as a law-specific interpolation over the sampled ranges. In particular, the height exponent is an effective finite-DCB exponent because varying h at fixed a_0 and K_0 changes Λ, η, and κ simultaneously; it is not a universal partial scaling with height. The fixed-η runs of Section 7.3 show that doubling or quadrupling η at fixed Λ changes L_0 by 4% or less for the cases checked; the exponents are still effective values along the sampled path, because κ changes with height and the deepest cases were not checked.

Section 7.1 shows that this law dependence is not random. Recast through Eq. (3), the eighteen fitted exponents become eighteen estimates of a single local slope s_j, and all of them fall inside the bracket [1/4, 1] set by the slender-beam and bulk limits [4, 21, 25, 26]. More than that, they order correctly: for every law the three sweeps return s values that decrease as the geometric-mean Λ they sample increases, which is consistent with the two limits, and the implied curvature is of the same magnitude in both intervals. The three one-factor sweeps are therefore consistent with a broad crossover interpretation of $F_j(\Lambda)$.

This reframing changes what the shape effect is. Within the common crossover the six laws do not move together, and the sense in which their window-averaged slopes differ is now specific: s_j rises monotonically or near-monotonically with the normalized post-peak area A_j, so a blunter post-peak branch places the same specimen further toward the bulk end of the crossover than a sharply decaying one does. Shape does not scale a common curve, which is what a transferable C_{shape} would require; it relocates the configuration along the crossover. This is why re-expressing the results in terms of ℓ_{ch} alone cannot remove the shape effect, and why the poor fit of a shared slope reported above was to be expected rather than anomalous. It suggests that integral properties of the post-peak branch are useful descriptors within this family: the rectangular and trapezoidal laws, whose A_j are 1.000 and 0.750, return s values within 0.002–0.023 of one another, whereas the trapezoidal and finite exponential laws, whose analytic forms are no more dissimilar, differ by 0.15–0.22. Because the rectangular and trapezoidal laws also share a constant-traction plateau, this pairing on its own does not separate area from form; the rank correlation across all six laws, which include post-peak branches with no plateau, supports the association but does not distinguish area, centroid, and final separation as causal descriptors.

These findings have direct implications for calibration and discretization. A law selected from global data alone may reproduce the structural curve while predicting a substantially different active-zone length. Likewise, a mesh chosen from a linear-law estimate will resolve different numbers of cohesive elements when another shape is used: the mean L_0 ranged from 0.59 times the linear value for REC to 2.22 times it for EXP, with individual EXP ratios up to 3.13. Mesh qualification should therefore be based on the shortest zone among the credible candidate laws, not solely on the law used for global calibration [28, 29]. Note that the zone measured here is the active zone at first debonding from a stationary tip. The three-element guideline of [28, 29] was derived for the steady-state propagation zone, which can be shorter, so a mesh that resolves the onset zone does not necessarily resolve propagation, and the zone ranking during propagation must be checked separately.

Finally, the penalty-stiffness and onset-threshold perturbations were small relative to the cross-law differences, and every law was evaluated over the same strength, toughness, and complete-height ranges. These checks support the comparison within their tested scope; so do the closed-form comparison of Section 7.2, the disclosed stabilization energies of the three rescued analyses, and the linear-geometry rerun; they do not replace a formal mesh-convergence study or experimental validation of the assumed cohesive shapes or reconstructed local fields.

9. Conclusions

This work isolated the effect of post-peak cohesive-law shape on Mode-I DCB debonding in a 100-case finite-element framework with an explicitly defined extraction procedure. Six laws sharing identical initial stiffness, cohesive strength, and fracture energy were driven to a common, interpolated debonding-onset event, and the process-zone length L_0 was recovered from every analysis by temporal and spatial interpolation.

Four conclusions follow. First, similar global responses can hide very different local zones: across the 16 six-law blocks, the onset-load spread was 1.9–11.8%, while the L_0 spread was 116–258%, 19–98 times larger. Part of this gap comes from the shared G_c; the more useful global result is the 11–16% drop of the onset load below the beam value, which follows the order of L_0. A matching load–opening curve therefore says little about the size of the process zone. Second, shape cannot be captured by a single multiplying constant. The order REC < TRAP < LIN < POLY < MULTI < EXP never changed, but a single shared exponent fitted much worse in all three sweeps; the exponents depended on the law, the adjacent-point slopes kept the largest-area and smallest-area laws apart in every interval, and C_{shape} had a coefficient of variation of 24–44% across the height range. Third, the three sets of exponents are still consistent with each other. Expressed as the local slope s of the dimensionless process-zone function, all eighteen values lie within [1/4, 1] set by the slender-beam and bulk limits and, for each law, follow the cohesive-length-to-height ratio of each sweep, which points to a broad crossover between the two limits. Within this crossover, s increases with the post-peak area: shape moves a case along the crossover rather than scaling a common curve, which is why no single coefficient works. Fourth, the added checks support these results: the penalty stiffness and onset threshold changed L_0 by less than 1% and 5%, respectively; the linear-law onset loads agree with the closed-form solution within 1% at h = 1.6 mm and 5% at h = 3.2–6.4 mm; the stabilization energy of the three stabilized runs is below 10^{-5} of the internal energy at the last saved frame; switching off bulk geometric nonlinearity changes the onset load by 0.1% and L_0 by 4%; the fixed-η runs change L_0 by at most 4%; and the shortest zone spans eight interface elements, more than twice the usual minimum.

In practice, calibration on global DCB data alone leaves the process-zone length, and thus the required element size, uncertain by a factor of about four across these laws. The mesh should be chosen for the shortest zone among the plausible laws, using the zone the analysis needs (the onset zone studied here, or the propagation zone, which may be shorter). Local measurements such as crack-tip opening or full-field data should be added to global curves when the process zone matters.

These conclusions are limited to monotonic Mode-I loading, linear-elastic adherends, the plane-strain DCB geometry studied (70 mm bonded length and, except for the fixed-η runs, a 30 mm precrack), the ranges $T_{\max}$ = 40–125 MPa, G_c = 0.05–0.20 N/mm, and h = 1.6–32 mm, and one-factor sweeps. They should not be extended to plastic adherends, mixed-mode or cyclic loading, or rate-dependent interfaces without further work, and the computed local fields still need experimental validation. Future work should combine full-field or crack-opening measurements with runs that vary several dimensionless groups at once, and extend the model to mixed-mode, cyclic, and rate-dependent loading.

Author Contributions

Not applicable.

Acknowledgments

Not applicable.

Conflict of Interest

The author has no competing financial or personal interests to declare in relation to this work.

Funding

No external funding was received for this work.

Data Availability Statements

The complete data set, the 100 Abaqus input decks, the six-law user-element source, the onset-extraction and regression scripts, and the per-case summary table, is available from the corresponding author on reasonable request.

Declaration of Generative AI and AI-Assisted Technologies in the Writing Process

During the preparation of this work the author used a generative artificial intelligence assistant to proofread the manuscript for language and internal consistency and to check the completeness and accuracy of the bibliographic references. After using this tool, the author reviewed and edited the content as needed and takes full responsibility for the content of the published article.

Nomenclature

A_j	Normalized post-peak area of law j
a_0	Initial (pre-)crack length
C_{shape}	Nominal beam shape coefficient
E, E′	Young's modulus; plane-strain modulus $E/(1-\nu^2)$
$f_j(\xi)$	Normalized post-peak traction function of law j
G_c	Critical fracture energy
h	Arm height
K_0	Initial (penalty) interface stiffness
L_0	Debonding-onset process-zone length
L_{cz}	Cohesive-zone length
$F_j(\Lambda)$	Dimensionless process-zone function L_0/h of law j
m_j, n_j, q_j	Fitted strength, energy, and height exponents
P, P_0	Load per unit width; its value at the interpolated onset event
s	Local logarithmic slope $\partial \ln F / \partial \ln \Lambda$ of the dimensionless process-zone function
S_P, S_L	Global and local shape sensitivity
T_{max}	Cohesive strength (maximum traction)
x, x_d, x_f	Axial coordinate; damage-front and failure-front positions

Greek symbols

α	Temporal interpolation factor
Δx	Interface-element length
δ	Interface opening; $\delta(x = 0)$ is the opening at the original crack tip
δ_0, δ_f	Opening at peak traction; final separation
η, κ, Λ, τ	Dimensionless groups $a_0/h, K_0 h/E', \ell_{ch}/h, T_{max}/E'$
ℓ_{ch}	Characteristic cohesive length $E' G_c / T_{max}^2$
ν	Poisson's ratio
ξ	Normalized post-peak separation coordinate
χ_j	Normalized post-peak energy centroid of law j

References

[1] Barenblatt, G.I., The Mathematical Theory of Equilibrium Cracks in Brittle Fracture, *Advances in Applied Mechanics*, 7, 1962, 55–129.
[2] Dugdale, D.S., Yielding of Steel Sheets Containing Slits, *Journal of the Mechanics and Physics of Solids*, 8, 1960, 100–104.
[3] Park, K., Paulino, G.H., Cohesive Zone Models: A Critical Review of Traction–Separation Relationships Across Fracture Surfaces, *Applied Mechanics Reviews*, 64, 2011, 060802.
[4] Hillerborg, A., Modéer, M., Petersson, P.E., Analysis of Crack Formation and Crack Growth in Concrete by Means of Fracture Mechanics and Finite Elements, *Cement and Concrete Research*, 6, 1976, 773–781.
[5] Chandra, N., Li, H., Shet, C., Ghonem, H., Some Issues in the Application of Cohesive Zone Models for Metal–Ceramic Interfaces, *International Journal of Solids and Structures*, 39, 2002, 2827–2855.
[6] Alfano, G., On the Influence of the Shape of the Interface Law on the Application of Cohesive-Zone Models, *Composites Science and Technology*, 66, 2006, 723–730.
[7] Gustafson, P.A., Waas, A.M., The Influence of Adhesive Constitutive Parameters in Cohesive Zone Finite Element Models of Adhesively Bonded Joints, *International Journal of Solids and Structures*, 46, 2009, 2201–2215.
[8] Campilho, R.D.S.G., Banea, M.D., Neto, J.A.B.P., da Silva, L.F.M., Modelling Adhesive Joints with Cohesive Zone Models: Effect of the Cohesive Law Shape of the Adhesive Layer, *International Journal of Adhesion and Adhesives*, 44, 2013, 48–56.
[9] Zhang, J., Wang, J., Yuan, Z., Jia, H., Effect of the Cohesive Law Shape on the Modelling of Adhesive Joints Bonded with Brittle and Ductile Adhesives, *International Journal of Adhesion and Adhesives*, 85, 2018, 37–43.
[10] Zhang, W., Lin, J., Huang, Y., Lin, B., Liu, X., State of the Art Regarding Interface Bond Behavior Between FRP and Concrete Based on Cohesive Zone Model, *Structures*, 74, 2025, 108528.
[11] Zhang, W., Huang, Y., Three-Dimensional Numerical Investigation of Mixed-Mode Debonding of FRP–Concrete Interface Using a Cohesive Zone Model, *Construction and Building Materials*, 350, 2022, 128818.
[12] Simon Portillo, F.J., Cuadrado Sempere, O., Marques, E.A.S., Sánchez Lozano, M., da Silva, L.F.M., Mechanical Characterisation and Comparison of Hyperelastic Adhesives: Modelling and Experimental Validation, *Journal of Applied and Computational Mechanics*, 8, 2022, 359–369.
[13] Xu, S., Zhao, C., Xiao, B., Wei, G., Kuang, N., Zhou, S., Zhang, W., Mechanism Based Four-Linear Cohesive Zone Model for Mode I Fracture of Different Stacking Sequence CFRP Laminates, *Theoretical and Applied Fracture Mechanics*, 134, 2024, 104693.
[14] Duan, Q., Hu, H., Cao, D., Cai, W., Li, S., A New Mechanism Based Cohesive Zone Model for Mode I Delamination Coupled with Fiber Bridging of Composite Laminates, *Composite Structures*, 332, 2024, 117931.
[15] Çelik, A., Özen, A., Anil, O., Mercimek, O., Failure Mechanism-Based Cohesive Modeling of TRM-Masonry Interface: A New Approach for Traction–Separation Laws, *Structures*, 87, 2026, 111736.
[16] Shirzadeh, Z., Fakoor, M., Daneshjoo, Z., Simulating Delamination in Composite Laminates with Fracture Process Zone Effects: A Novel Cohesive Zone Modeling Approach, *Engineering Fracture Mechanics*, 315, 2025, 110834.
[17] Calvo, J.V., Quiñonero-Moya, A.R., Feito, N., Tarancón, J.E., Giner, E., Sensitivity of Cohesive Zone Models in CFRP Delamination Modeling, *Theoretical and Applied Fracture Mechanics*, 143, 2026, 105423.
[18] Hai, L., Feng, Y., A Phase-Field Cohesive Fracture Model Free from the Length Scale Constraints, *Computer Methods in Applied Mechanics and Engineering*, 447, 2025, 118374.
[19] Valoroso, N., de Barros, S., Adhesive Joint Computations Using Cohesive Zones, *Applied Adhesion Science*, 1, 2013, 8.
[20] Sauvage, J.B., Chalandon, P., Poquillon, D., Nardin, M., Aufray, M., Using the Finite Element Analysis Method to Study the 3-Point Bending Test for the Characterization of the Adherence, *Journal of Applied and Computational Mechanics*, 6, 2020, 505–516.
[21] Williams, J.G., Hadavinia, H., Analytical Solutions for Cohesive Zone Models, *Journal of the Mechanics and Physics of Solids*, 50, 2002, 809–825.
[22] Li, G., Li, C., Linking Bilinear Traction Law Parameters to Cohesive Zone Length for Laminated Composites and Bonded Joints, *Advances in Aircraft and Spacecraft Science*, 1, 2014, 177–196.
[23] Li, G., Li, C., Assessment of Debond Simulation and Cohesive Zone Length in a Bonded Composite Joint, *Composites Part B: Engineering*, 69, 2015, 359–368.
[24] Xie, J., Waas, A.M., Rassaian, M., Closed-Form Solutions for Cohesive Zone Modeling of Delamination Toughness Tests, *International Journal of Solids and Structures*, 88–89, 2016, 379–400.
[25] Soto, A., González, E.V., Maimí, P., Turon, A., Sainz de Aja, J.R., de la Escalera, F.M., Cohesive Zone Length of Orthotropic Materials Undergoing Delamination, *Engineering Fracture Mechanics*, 159, 2016, 174–188.
[26] Azab, M., Parry, G., Estevez, R., An Analytical Model for DCB/Wedge Tests Based on Timoshenko Beam Kinematics for Accurate Determination of Cohesive Zone Lengths, *International Journal of Fracture*, 222, 2020, 137–153.
[27] Azab, M., Estevez, R., Houda, M., Parry, G., Influence of the DCB/Wedge Beam Kinematics on the Identification of the Cohesive Parameters of Interfaces, *International Journal of Solids and Structures*, 252, 2022, 111810.
[28] Turon, A., Dávila, C.G., Camanho, P.P., Costa, J., An Engineering Solution for Mesh Size Effects in the Simulation of Delamination Using Cohesive Zone Models, *Engineering Fracture Mechanics*, 74, 2007, 1665–1682.
[29] Harper, P.W., Hallett, S.R., Cohesive Zone Length in Numerical Simulations of Composite Delamination, *Engineering Fracture Mechanics*, 75, 2008, 4774–4792.
[30] Ai, X., Chen, B., Kassapoglou, C., Structural Cohesive Element for the Modelling of Delamination in Composite Laminates without the Cohesive Zone Limit, *Engineering Fracture Mechanics*, 329, 2025, 111586.
[31] Anam, K., Todt, M., Pettermann, H.E., An Efficient Ply-Level Based Modeling Strategy for Predicting Delamination Behavior in Laminated Composites, *Journal of Applied and Computational Mechanics*, 10, 2024, 652–658.
[32] Škec, L., Identification of Parameters of a Bi-Linear Cohesive-Zone Model Using Analytical Solutions for Mode-I Delamination, *Engineering Fracture Mechanics*, 214, 2019, 558–577.
[33] Li, G., Analytical Estimation of Cohesive Parameters for a Bilinear Traction-Separation Law in DCB Mode I Loading, *Journal of Mechanics of Materials and Structures*, 18, 2023, 293–317.
[34] Arrese, A., Boyano, A., De Gracia, J., Mujika, F., A Novel Procedure to Determine the Cohesive Law in DCB Tests, *Composites Science and Technology*, 152, 2017, 76–84.
[35] Gorman, J.M., Thouless, M.D., The Use of Digital-Image Correlation to Investigate the Cohesive Zone in a Double-Cantilever Beam, with Comparisons to Numerical and Analytical Models, *Journal of the Mechanics and Physics of Solids*, 123, 2019, 315–331.
[36] Huo, X., Luo, Q., Li, Q., Zheng, G., Sun, G., On Characterization of Cohesive Zone Model (CZM) Based upon Digital Image Correlation (DIC) Method, *International Journal of Mechanical Sciences*, 215, 2022, 106921.

ORCID iD

Marc Azab https://orcid.org/0000-0003-0173-3209

How to cite this article: Azab M., Law-Dependent Cohesive-Zone Scaling in Mode-I Double-Cantilever-Beam Debonding, *J. Appl. Comput. Mech.*, xx(x), 2026, 1–15. https://doi.org/10.22055/jacm.2026.49649.6131